

Flexural fatigue behaviour of a heated ultra-high-performance fibre-reinforced concrete

José D. Ríos¹, Héctor Cifuentes^{1*}, Sergio Blasón², Manuel López-Aenlle², Antonio Martínez-De La Concha¹

¹Department of Continuum Mechanics and Structural Analysis. School of Engineering, University of Seville, Spain

²Department of Construction and Fabrication Engineering. University of Oviedo, Spain

*Corresponding author: bulte@us.es (Héctor Cifuentes)

Abstract

A comprehensive experimental campaign was carried out to assess the flexural fatigue behaviour of an ultra-high-performance fibre-reinforced concrete. Several concrete mixes were submitted to room temperature, 100 °C, 200 °C, and 300 °C. Two types of reinforcement were explored: steel fibres and a combination of steel and polypropylene fibres. The influence of the addition of fibres and the temperatures in the microstructure were analysed through X-ray CT scans. In addition, the mechanical and fracture properties of the concrete were determined with monotonic tests and a connection between macroscopic and microscopic results was established to explain the fatigue behaviour. The beneficial effect of the fibres was observed essentially at a low cyclic fatigue regime. In heated concretes, the reduction of matrix porosity due to the presence of steel fibres led to significant damage after being exposed to 300 °C by spalling failure. By contrast, the concrete reinforced with polypropylene fibres maintained remarkably similar fatigue behaviour at room temperature and 300 °C.

1. Introduction

The fatigue behaviour of cementitious materials has been studied for a hundred years in plain concrete, especially under compression [1–5] and bending [6–9]. However, the interest in the fatigue behaviour of concrete has grown significantly since the addition of steel fibres [10–17] in the concrete matrix and the development of high-strength concrete [18–23]. Such enhanced materials are mostly used in infrastructures where time-variable loadings are predominant (e.g., bridge decks, pavements, high-speed railways, high-rise buildings, off-shore structures) [12,24]. Fibre reinforcement leads to a higher deformation capacity, which in turn improves fatigue life [17,24–26]. Nevertheless, the presence of fibres in the concrete results in a more heterogeneous matrix, which can be a source of defects [25,27]. The heterogeneity of the concrete matrix and its inherent flaws (i.e., porosity, entrapped air, and microcracks) lead to a progressive deterioration of the microstructure when the material is subjected to cyclic loading. This causes a steady decrease in the stiffness of the material, which commonly results in fatigue failure [25,28].

In ultra-high-performance fibre-reinforced concrete (UHPFRC), the matrix is essentially characterised by the use of components with significant small-size particles (e.g., silica fume,

38 fly ash, ground granulated blast furnace slag), which promotes higher particle packing [29,30],
39 and a remarkably low water-to-binder ratio [31,32]. Both features lead to a dense concrete
40 matrix (i.e., with low porosity) and a significant enhancement of mechanical properties and
41 durability [33–35]. Nonetheless, this produces more brittle material which commonly requires
42 reinforcement through the addition of a large number of steel fibres in the concrete matrix to
43 provide higher strain capacity [25,31,36–38]. As a result, the microstructure of UHPFRC
44 becomes significantly more heterogeneous and prone to have additional defects due to fibre
45 addition which influence fatigue behaviour [25]. On the other hand, the excellent mechanical
46 properties of UHPFRC have made it possible to reduce the weight of structures by being able
47 to build slenderer elements for the same acting loads [19,22]. Hence, permanent loads
48 decrease whereas live loads (e.g., wind, earthquakes, sea waves) represent a more significant
49 percentage of the total loads [19,22]. As a result, such structures are more sensitive to fatigue
50 failure than those built with conventional or high-strength concrete [19].

51 Nevertheless, in some applications, UHPFRC must be capable of bearing thermal and
52 mechanical loads for long periods. Some examples are the containment of steam or molten
53 salts, as well as thermal energy storage systems with a solid medium in which the concrete
54 directly accumulates the thermal energy [39–41]. These structures must bear heating and
55 cooling for long periods of time, which generates fatigue damage and eventually leads to
56 premature failure [42,43]. In these applications, the stability of concrete is crucial to withstand
57 temperatures without being significantly degraded, which would affect the strength of the
58 material. The heating of concrete generates evaporation of free water, dehydration, and even
59 the decomposition of the matrix at high temperatures [39,44–46]. If internal stresses due to
60 the thermal gradients and high steam pressure exceed the tensile strength of concrete, crack
61 generation occurs in the matrix, resulting in a degradation of the material's performance
62 [39,47–49]. In dense concrete mixes, such as UHPFRC, high steam pressure leads to a more
63 severe deterioration of the matrix than in more porous concretes (i.e., conventional or high-
64 strength concrete) because the steam cannot be easily released through the pore connections
65 [46,50]. As a result, the degradation of the concrete matrix by thermal damage exerts a
66 notable influence on the mechanical properties and fatigue behaviour of UHPFRC.

67 To date, studies on the fatigue behaviour of UHPFRC are scarce despite the increasing interest
68 in this concrete and its many possible applications in which cyclic loading is predominant (e.g.,
69 offshore structures, slenderer bridge decks and piers, airport pavements, machine
70 foundations, wind turbine towers) [25,35]. Most research has focused essentially on
71 determining fatigue strength (i.e., endurance limit) in bending [32,33] and uniaxial tension
72 [35,51] due to the extraordinary improvement of tensile strength in this concrete. Moreover,
73 few studies have dealt with the influence of fibres on the fatigue life of UHPFRC [25,27]. In
74 fact, it is known that the concrete matrix (i.e., components, amount and fibre distribution, and
75 inherent flaws) plays a primary role in the fatigue behaviour of concrete under cyclic loading
76 [25]. However, few studies have focused on establishing a relationship between the pore
77 structure of the matrix and its degradation due to thermal damage, exploring the contribution
78 of fibre reinforcement to the mechanical properties and the fatigue performance of UHPFRC at
79 different temperatures.

80 Our study focused on the influence of the pore structure of the concrete matrix on the fatigue
81 behaviour of UHPFRC subjected to heating (i.e., room temperature, 100 °C, 200 °C, and 300
82 °C). A comprehensive experimental campaign was conducted to determine the fatigue
83 strength (i.e., endurance limit) of a UHPFRC and its corresponding non-reinforced concrete
84 with three-point bending fatigue tests in notched specimens. The goal was to obtain the S-N
85 field at room temperature (RT), 100 °C, 200 °C, and 300 °C. A probabilistic fatigue model based
86 on the Weibull distribution functions developed by Castillo and Fernández-Canteli [52,53] was
87 used to determine the S-N field. Previously, static three-point bending tests were performed to
88 determine the mechanical properties of the concrete under static loadings at the different
89 temperatures tested. The influence of the addition of fibres and the temperature on the
90 microstructure and consequently on the mechanical properties and fatigue behaviour was
91 determined through an X-ray computed tomography (CT) scan. Moreover, the concrete matrix
92 was analysed with a thermoanalytical test from room temperature to 400 °C to determine the
93 dehydration or decomposition produced by the heating. The results of the X-ray CT scan and
94 the thermoanalytical methods used were obtained from a previous paper by the authors that
95 explored the mechanical and fracture properties of the same heated UHPFRC [48]. Finally, a
96 connection was established between the results of the X-ray CT scan, the thermoanalytical
97 methods, the mechanical properties, and the fatigue behaviour at the various temperatures
98 tested.

99 **2. Mix proportions and specimen preparation**

100 Three ultra-high-performance fibre-reinforced concretes were manufactured in this study.
101 They were all properly prepared with the same constituents and only differed in the type of
102 fibres added. The dosage of mixes was designed in accordance with the methodology
103 proposed by Deeb et al. [54], adapted to the materials available in our area. The binder was
104 composed of CEM I 52.5 R/SR; the silica fume had a particle size under 0.1 µm, and the ground
105 granulated blast furnace slag (GGBS) had a maximum particle size under 60 µm. Two types of
106 quartz sand were used as aggregate. The fine aggregate was characterised by a maximum
107 particle size of 315 µm, with a median particle size of 136.9 µm and a fineness modulus of
108 0.48. The coarse aggregate had a maximum particle size of 800 µm, with a median particle size
109 of 297.3 µm and a fineness modulus of 2.36. The grain-size distribution of the aggregates is
110 shown in Table 1. A highly active superplasticizer based on polycarboxylic ether was used to
111 save water.

117

Table 1: Grain-size distribution of the coarse and fine aggregate

Sieve-size (μm)	Coarse aggregate (% mass retained)	Fine aggregate (% mass retained)
800	0.0	0.0
630	0.5	0.0
500	5.0	0.0
400	18.0	0.0
315	38.0	0.0
250	82.0	4.0
150	92.6	44.7
100	97.9	65.0
80	100.0	85.0
63	100.0	95.0
40	100.0	100.0

118

Table 2: Nomenclature, constituent, and mix proportions

Constituents	Mixes (kg/m^3)		
	RC	UFC	UFC_PP
cement	544	544	544
silica fume	214	214	214
GGBS	312	312	312
quartz sand (< 0.315 mm)	470	470	470
quartz sand (< 0.800 mm)	470	470	470
superplasticizer	42	42	42
short steel fibres	-	98	98
long steel fibres	-	98	98
PP fibres	-	-	1.2
water/cement	0.34	0.34	0.34
water/binder	0.17	0.17	0.17
bulk density	2,198 (19)	2,404 (20)	2,342 (27)

119

120 The first concrete we designed, labelled as UFC (ultra-fibre concrete), was reinforced with two
 121 types of steel fibres exclusively. The shorter fibres had a straight shape, were 13 mm in length,
 122 and 0.2 mm in diameter, and had a yield strength of 2,750 MPa. The longer fibres had a
 123 hooked-end shape, were 30 mm in length and 0.38 mm in diameter, and had a yield strength
 124 of 3,070 MPa. The fibre content was 2.5% in volume fraction and both types of fibres were
 125 combined at 50% (1.25% short fibres and 1.25% long fibres). The second concrete, labelled as
 126 UFC_PP (ultra-fibre concrete with polypropylene), contained identical types and proportions of
 127 steel fibres as the UFC, with the addition of polypropylene (PP) fibres. The PP fibres were 24
 128 mm in length and 31 μm in diameter. A plain concrete mix with the same constituents was
 129 manufactured to be used as reference concrete (RC). The mix proportions of each type of mix
 130 are shown in Table 2. The selection of the types of fibres and their mix proportions used in this
 131 research was in accordance with the effectiveness criteria for UHPFRC from a mechanical

132 behaviour perspective and the cost of fibres, which were comprehensively studied by the
133 authors in previous research. For more information, see [31,55,56].

134 The chemical composition of cementitious materials is shown in Table 3. The cement was
135 essentially composed of SiO₂, CaO, and a higher content of SO₃ than conventional cement due
136 to its sulphur-resistant feature. The silica fume comprised 90% of particles under 0.1 µm and
137 had a SiO₂ content above 90%. The GGBS primarily included SiO₂ and CaO.

138 **Table 3: Chemical composition of cementitious materials**

composition % (mass)	cement ^a	silica fume	GGBS
CaO	66.07	0.21	51.14
Al ₂ O ₃	3.22	0.43	9.12
SiO ₂	18.96	95.63	28.12
Fe ₂ O ₃	4.62	0.10	0.42
MgO	1.50	0.39	6.06
SO ₃	3.00	0.04	1.77
K ₂ O	0.20	0.79	0.54
N ₂ O	0.14	0.00	0.00
Na ₂ O	0.27	0.20	0.19
TiO ₂	0.00	0.00	0.00
LOI		1.84	1.47

139 ^a Type I cement 52.5 R/SR

140 All specimens were manufactured following the same procedure. The casting procedure and
141 mixing time were optimal to achieve a mix that was fluid enough. Mixing time essentially
142 depends on the grain-size aggregate and the power of the mixing rotation [57]. First, all dry
143 constituents were poured into the mixer and rotated for 2 min. Next, the water-
144 superplasticizer solution was added and rotated for 30 min until a fluid and homogeneous mix
145 was obtained. Finally, the fibres were poured into the mixer and rotated for 10 min until they
146 were efficiently dispersed. After this, the moulds were filled by moving the bucket with the
147 concrete mass uniformly from side to side to obtain the most homogeneous concrete possible.
148 The specimens were subsequently unmoulded after being cured for 24 h and then immersed in
149 water at 20 °C for 28 days.

150

151

152

153 **3. Experimental programme**

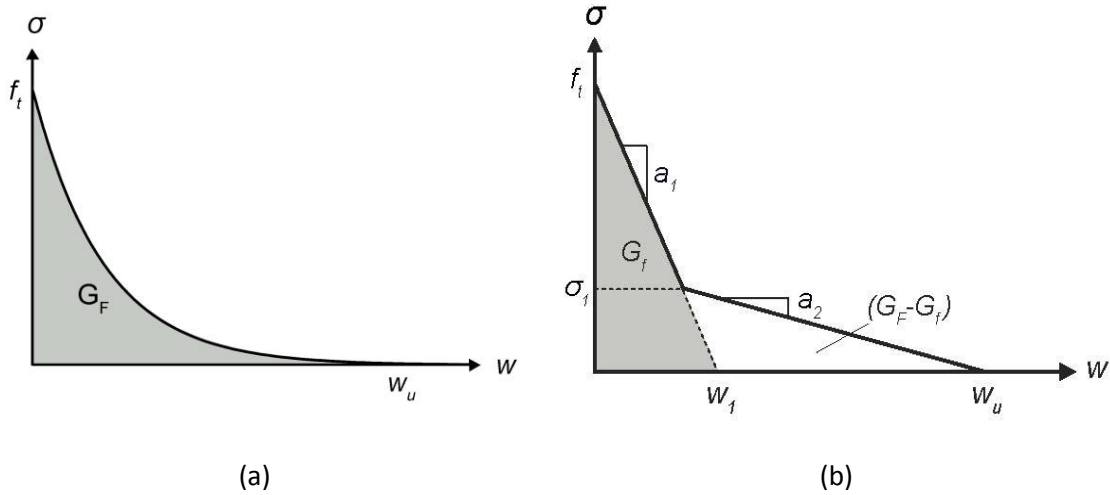
154 **3.1 Mechanical and fracture tests**

155 Cubic specimens with a side of 100 mm, cylinders 100 mm in diameter and 200 mm in height,
156 and prismatic specimens 100×100×440 mm³ were cast in order to determine their mechanical
157 and fracture properties. RC and UFC concrete were tested at room temperature, 100 °C, 200
158 °C, and 300 °C; and UFC_PP was tested at room temperature and 300 °C.

159 **3.1.1 Testing of specimens at room temperature**

160 Compressive strength was determined in four cubic specimens for each mix (i.e., RC, UFC, and
161 UFC_PP) according to the EN 12390-3 standard [58]. Young's modulus was measured in four
162 cylinders for every mix according to the EN 12390-13 standard [59]. This test implied gradually
163 loading the specimen up to a third of its failure load and recording its relative strain with two
164 linear variable displacement transducers (LVDTs) 25 mm in length that faced each other and
165 surrounded the cylinder. Three-point bending tests on four notched prismatic specimens for
166 every mix were performed to measure the work-of-fracture according to the RILEM method
167 [60]. All specimens had a notch-to-depth ratio of one-sixth. The mid-span deflection was
168 measured with a 25-mm LVDT mounted on a rigid frame to prevent torsional effects and a clip
169 gauge at the bottom of the specimen to measure the crack mouth opening displacement
170 (CMOD).

171 A two-dimensional finite element (FE) model created by the authors [56] was used to
172 reproduce the fracture process in the three-point bending tests. The model consisted of the
173 ligament area, modelled with 4-node two-dimensional cohesive elements (COH2D4), and the
174 rest of the sample, which was meshed with 3-node tetrahedral solid elements (CPEG3) with
175 linear behaviour and generalised plane strain. The cohesive elements were defined by an
176 exponential separation law characterised by the maximum stress (f_t), the exponential
177 parameter, and the displacement at failure (w_u ; see Figure 1.a). The solid elements were
178 defined as assuming elastic-plastic behaviour. Young's modulus was determined
179 experimentally and Poisson's ratio was assumed to be 0.2 in all cases. The exponential
180 cohesive parameters were determined to establish an agreement between the results of the
181 experimental load-deflection curves and the FE load-deflection curves. Finally, the bilinear
182 cohesive separation laws of each test were determined by a numerical fitting from the
183 exponential laws.



184 **Figure 1: Cohesive law of fracture process: exponential (a) and bilinear (b)**

185 **3.1.2 Testing of specimens in heated conditions**

186 The specimens were heated at a rate of 10 °C/min and the target temperature was maintained
 187 for at least 24 hours to ensure a homogeneous temperature in the material. The type of tests
 188 and the number of specimens tested were the same as for room temperature. However, the
 189 high temperature prevented the use of sensors in these tests. The three-point bending tests
 190 for every mix at the temperatures selected (100 °C, 200 °C and 300 °C) were carried out in a
 191 furnace specifically designed to introduce the actuator and supporting framework inside the
 192 chamber during the testing procedure. Thus, it was possible to test the specimens at the target
 193 temperature. Nevertheless, it was only possible to record load and actuator position data due
 194 to the high temperatures. To estimate the load-deflection curves from the three-point bending
 195 tests at various temperatures (100 °C, 200 °C and 300 °C), it was assumed that the difference
 196 between the deflection and the actuator displacement was due to the fact that the machine
 197 underwent a strain during the loading process. Hence, a conversion factor was established
 198 between the deflection and actuator displacement at RT. Finally, the deflection at any
 199 temperature was estimated from the actuator displacement and conversion factor. For more
 200 detailed information, see Ríos et al. [48].

201 **3.2 Fatigue tests**

202 Fourteen prismatic specimens 100×100×440 mm³ for each fatigue test (i.e., mixes and
 203 temperatures) were manufactured in order to determine fatigue life. Three-point bending
 204 fatigue tests in notched prismatic specimens were performed with a notch-to-depth ratio of
 205 one-sixth. Fatigue tests were conducted in a servo-hydraulic machine with a maximum loading
 206 capacity of 150 kN. All tests were carried out with the same stress ratio (0.2) for a varying
 207 maximum load and a loading frequency of 4 Hz. The reference concrete (RC) and steel fibre-
 208 reinforced concrete (UFC) were exposed to room temperature, 100 °C, 200 °C and 300 °C;
 209 finally, the steel-PP fibre-reinforced concrete (UFC_PP) was exposed to room temperature and
 210 300 °C. All fatigue tests were carried out in heated specimens inside the furnace at the target
 211 temperature.

212 From the experimental fatigue data, the probabilistic fatigue model developed by Castillo and
213 Fernández-Canteli [61] was used to estimate the S-N field. The fatigue model, based on the
214 Weibull distribution functions, defines the S-N field as hyperbolic curves that represent the
215 same probability of failure (i.e., percentiles). The model can be adapted to any general fatigue
216 reference parameter – the driving force – that characterises the damage progress criterion
217 (e.g., stress, strain, energetic parameters). The probability of failure is calculated as follows:

$$218 \quad P_{fail} = 1 - \exp \left[- \left(\frac{V - \lambda}{\delta} \right)^\beta \right] \quad (1)$$

219 in which

$$220 \quad V = (\log GP - C)(\log N_{ini} - B) \quad (2)$$

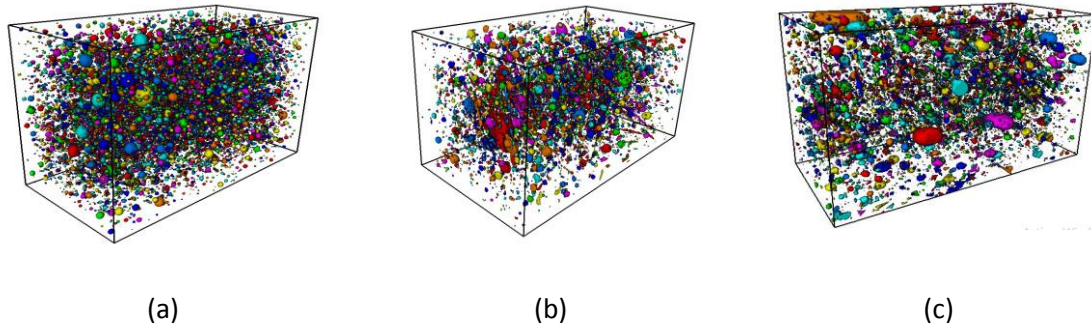
221 where V is the normalized parameter, GP is the damage generalized parameter, N_{ini} is the
222 lifetime and λ , β and δ are the location, shape and scale parameters of the Weibull
223 distribution, respectively. In this study, the generalized damage parameter used was the stress
224 level (S), defined as f/f_r , where f was the flexural stress applied and f_r was the monotonic
225 flexural strength resulting from the three-point bending tests.

226 The location parameter represents the smallest value of V at which failure may occur. Both
227 scale (δ) and shape (β) are parameters related to the scattering of experimental results. The
228 former is related to the specimen size and the latter corresponds to the fracture mechanism.
229 For more detailed information about the probabilistic fatigue model used, see [61].

230 **3.3 X-ray computed tomography analysis**


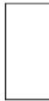



231 The X-ray computed tomography technique was used to determine the porosity of the
232 concrete matrix at room temperature due to entrapped air during the mixing process and the
233 influence of temperature on pore structure at 300 °C. We used the XYLON Y. Cougar SMT X-ray
234 inspection equipment housed in the Characterisation Service of the University of Seville, Spain.
235 The equipment contains a multi-focus tube and wolfram target which allows the inspection in
236 the range between 25-160 kV and 0.01-1 mA intensity. It can generate images with a
237 geometric magnification up to 2,000×. The X-ray graphs are reconstructed and processed with
238 VGStudio MAX 2.2.3 software. The specimens submitted to the X-ray test were sawn and
239 extracted from the core of the prismatic specimens (100×100×440 mm³) to avoid boundary
240 effects. The dimensions of the samples were approximately 25×25×100 mm³. Four samples of
241 each mix (RC, UFC and UFC_PP) were analysed at the temperatures on both ends of the
242 spectrum (RT and 300 °C). The samples were scanned at RT and after being subjected to 300
243 °C. Only the samples subjected to the highest temperatures (RT and 300 °C) were scanned and
244 intermediate behaviour was assumed to happen at 100 °C and 200 °C. The 2D X-ray
245 radiographs had a resolution of 1024×1024 pixels. These images were digitally reconstructed
246 (Figure 2) into 3D absorption contrast images of the sample providing 3D information about
247 areas with different density. A resolution of 40 μm in the three Cartesian directions was
248 obtained for these samples and mixes. For more detailed information about the procedure of

249 analysis, see [31]. A summary with the number and dimensions of the specimens cast as well
 250 as the properties determined at each temperature can be seen in Table 4.



251 **Figure 2: Pore distribution in specimens after 3D reconstruction: (a) RC at RT, (b) UFC at RT and (c)**
 252 **UFC_PP at RT.**

253 **Table 4: Summary of the types of specimens and their properties**

Specimen	Test °C	RC				UFC				UFC_PP	
		RT	100	200	300	RT	100	200	300	RT	300
 cube 100 mm side	f_c	4	4	4	4	4	4	4	4	4	4
 cylinder 100 diam. x 200	E_c	4	4	4	4	4	4	4	4	4	4
 prism 100x100x440mm ³	$f_{t1}, G_F,$ $\sigma_v, \alpha_1,$ $\alpha_2,$ $w_{1s},$ w_u	4	4	4	4	4	4	4	4	4	4
 prism 100x100x440mm ³	S-N	14	14	14	14	14	14	14	14	14	14
 prism 25x25x100mm ³	X-ray CT	4	4	4	4	4	4	4	4	4	4

254 3.4 Thermoanalytical tests and mineral composition

255 Thermogravimetric analysis (TGA), differential thermal analyses (DTA) and differential scanning
 256 calorimetry (DSC) were carried out with a TGA instrument. Alumina was used as reference
 257 material and samples were placed on crucibles for the tests. The analyses were performed at
 258 ambient air temperature during the entire heating period and the temperature was increased
 259 from room temperature to 350 °C at a rate of 10 °C/min.

260 The mineral composition of plain concrete (RC) after 28 days was determined by the X-ray
 261 diffraction technique and is shown in [48,62]. As can be seen in [48,62], the cement hydration
 262 process generated a pozzolanic reaction between the significant amount of SiO₂ (silica fume)
 263 and Ca(OH)₂, generating much C-S-H gel and reducing Ca(OH)₂ and CaCO₃ content [46,63].

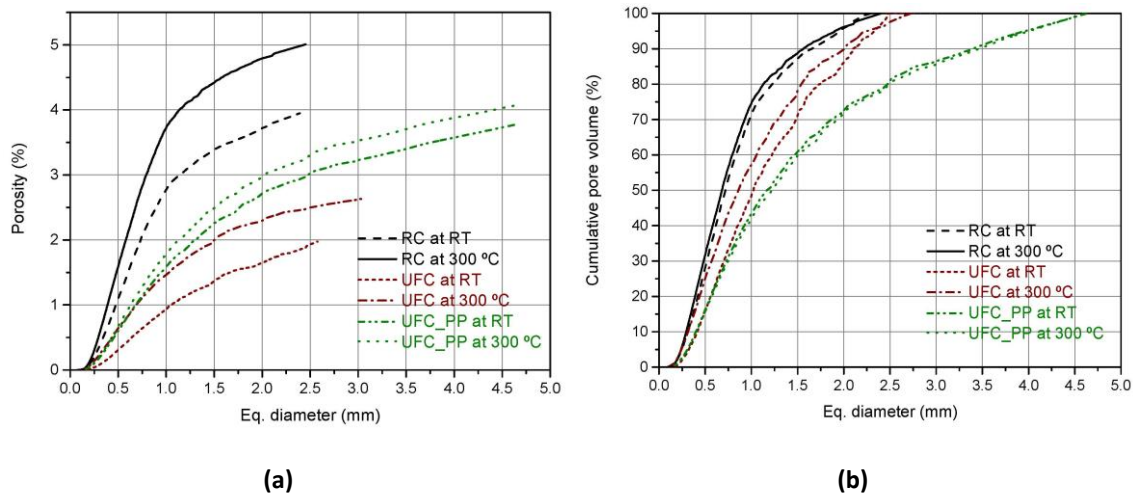
264

265 **4. Results and discussion**

266 **4.1 Porosity analysis with 3D X-ray CT images**

267 The evolution of porosity and cumulative pore volume with regard to the equivalent diameter
268 size distribution are shown in Figure 3.a and b, respectively. Figure 4 illustrates the pore
269 density related to the equivalent diameter size. The results for each mix (RC, UFC, and UFC_PP)
270 at room temperature and 300 °C are presented. The X-ray CT data used were previously
271 obtained by Ríos et al. [56].

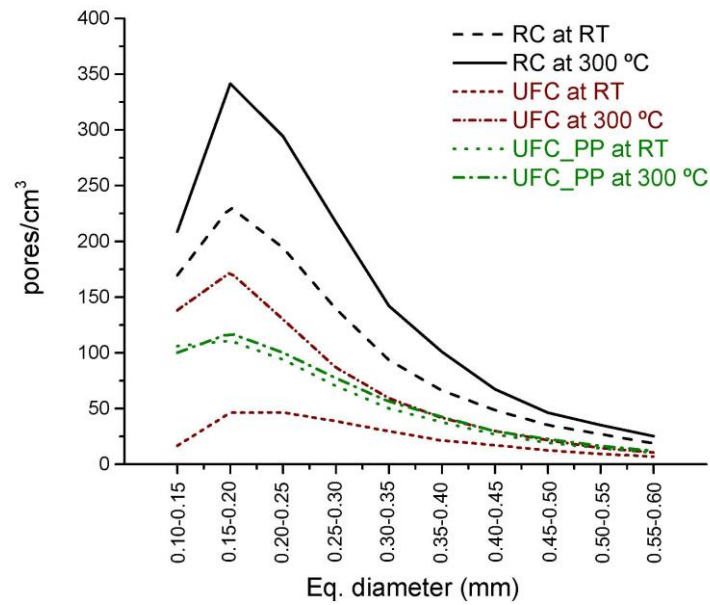
272 With regard to porosity at room temperature, Figure 2 shows that the presence of steel fibres
273 reduced porosity from 4.0% for the reference concrete (RC, that is, plain concrete) to 2.0% and
274 3.6% in UFC and UFC_PP respectively. This is consistent with the results obtained by other
275 authors [64,65]. The reduction in porosity was due to the fact that steel fibres burst the
276 entrapped air bubbles (with pores above 10 µm) in the concrete paste during the mixing
277 process [64] when the number of fibres was high. This is consistent with the results obtained
278 by Ponikiewski et al. [65] and Ríos et al. [31] and the decrease of pore density curves observed
279 in Figure 4. Additionally, the presence of fibres (PP or steel fibres) increased pore size due to
280 the water adsorption effect on the fibre surfaces, as observed in Figure 3.b, where fibre-
281 reinforced mixes (UFC and UFC_PP) reached larger pore sizes for the same cumulative pore
282 volume. This is also consistent with the results obtained by other authors [44,66]. Hence, the
283 porosity of the combined PP and steel fibre-reinforced concrete (UFC_PP) was higher than that
284 of concrete reinforced exclusively with steel fibres (UFC) because the fibre content (PP and
285 steel fibres) was higher and PP fibres induced entrapped air bubbles but did not burst them.



286 **Figure 3: Equivalent diameter size distribution versus (a) porosity and (b) cumulative pore volume**

287 Results of the porosity of all mixes at 300 °C (Figure 3.a) were higher than those obtained at
288 room temperature. Specifically, the RC mix (plain concrete) showed a 1% increase and was the
289 one most affected by the temperature; the UFC mix showed a 0.6% increase, and the UFC_PP
290 showed a 0.4% increase. The heating inflicted damage that increased the porosity mainly due
291 to the high vapour pressure generated by the moisture evaporation from 20 °C to 250 °C and
292 the dehydration of the C-S-H gel between 250 °C and 300 °C. This was based on the thermal

293 analyses previously carried out in the same concrete matrix by Ríos et al. [48]. In the PP fibre-
 294 reinforced mix (UFC_PP), porosity also increased due to the melting of PP fibres at around 165
 295 °C [44]. Note that the thermal damage inflicted affected pore sizes around 0.15-0.20 mm the
 296 most and its effect was negligible at pore sizes above 0.55 mm, as observed in Figure 4. This is
 297 because the stresses induced in the concrete matrix by thermal effects (moisture evaporation
 298 and dehydration) reach higher levels in smaller pores. Note that the PP fibre-reinforced
 299 concrete (UFC_PP) was the only mix in which the heating process did not significantly damage
 300 the microstructure compared to its status at room temperature, as concluded from the results
 301 shown in Figure 3 and Figure 4.



302
303 **Figure 4: Equivalent diameter size distribution represented by pore density**

304 4.2 Mechanical properties and fracture energy

305 The mechanical and fracture properties of each mix and temperature tested are presented in
 306 this subsection. As mentioned above, the PP fibre-reinforced mix (UFC_PP) was exclusively
 307 tested at room temperature and 300 °C. It was not possible to determine the fracture energy
 308 (G_f) of plain concrete (RC) at 100 °C, 200 °C, and 300 °C because the CMOD clip gauge
 309 transducer would not work correctly in high-temperature tests.

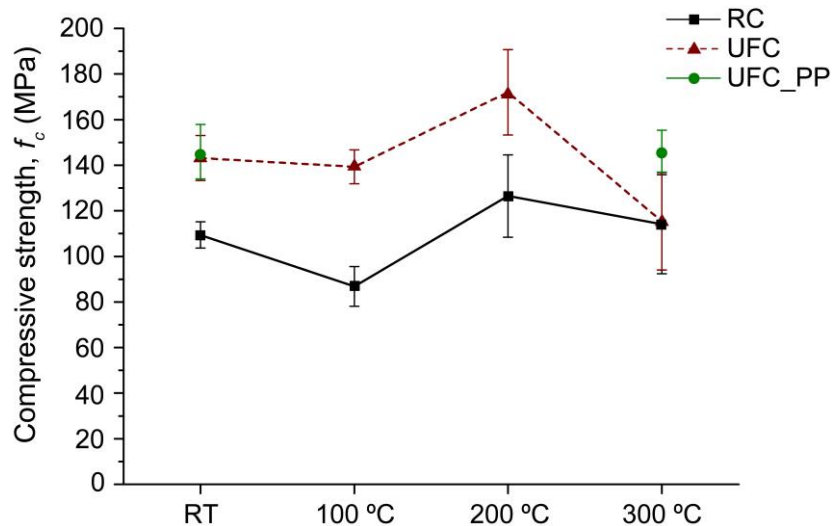
310 4.2.1 Compressive strength (f_c)

311 Based on the results at room temperature, fibre-reinforced mixes (UFC and UFC_PP) exhibited
 312 a remarkable improvement in compressive strength (f_c) compared to that of RC (plain
 313 concrete), with an average increase of 31% in UFC and 33% in UFC_PP. This improvement was
 314 essentially due to the beneficial sewing effect of the steel fibres, which limited the micro-
 315 cracking generated in the concrete during the compression tests [67]. Additionally, total
 316 porosity was considerably lower than that of RC (Figure 3.a) and more uniformly distributed
 317 (see Figure 3 and Figure 4). As can be observed, the presence of PP fibres in the concrete

318 matrix resulted in higher total porosity (Figure 3.a). However, it did not show a clear influence
319 on compressive strength, which agrees with the results obtained by other authors [45,68].

320 At 100 °C, compressive strength decreased in RC (21%) and UFC (2.6%) due to the high pore
321 pressure induced by the evaporation of moisture. When stresses reach tensile strength,
322 microcracks are generated in the concrete matrix, resulting in strength loss [43,44,69]. The
323 decrease was more significant in RC because pore pressure is more detrimental in small-size
324 pores [70] and the porosity of the RC mix was essentially characterised by having the smallest
325 size pores (see Figure 3 and Figure 4). At 200 °C, two simultaneous and contradictory effects
326 took place: the temperature of the cement paste improved its hydration [44,71,72] and the
327 high vapour pressure damaged the concrete matrix. The first effect resulted in the maximum
328 compressive strength, with an average value of 172 MPa (an increase of 20%) in the fibre-
329 reinforced concrete (UFC) and an increase of 15.6% in the RC mix. At 300 °C, the matrix
330 revealed considerable damage due to dehydration of the C-S-H gel [48]. Indeed, some samples,
331 even those reinforced exclusively with steel fibres (UFC), experienced an explosive failure in
332 the furnace during the heating process. Nonetheless, spalling failure was not observed in PP
333 fibre-reinforced concrete (UFC_PP) since PP fibres were melted and generated a network of
334 channels through which vapour could be evacuated more efficiently, mitigating the
335 detrimental effect of heating of the concrete matrix. Note that the scattering of results
336 increased with the rise in temperatures, showing that thermal gradients do not induce uniform
337 damage throughout the concrete matrix (Figure 5). By contrast, the fibre-matrix bond strength
338 played a crucial role in compressive strength. However, the expansion effect of steel fibres
339 embedded in the concrete matrix did not generate significant cracks below 400 °C, which is
340 consistent with other studies [72]. Hence, the appropriate fibre-concrete bond strength was
341 not noticeably degraded in the temperature interval used in this research.

342



343

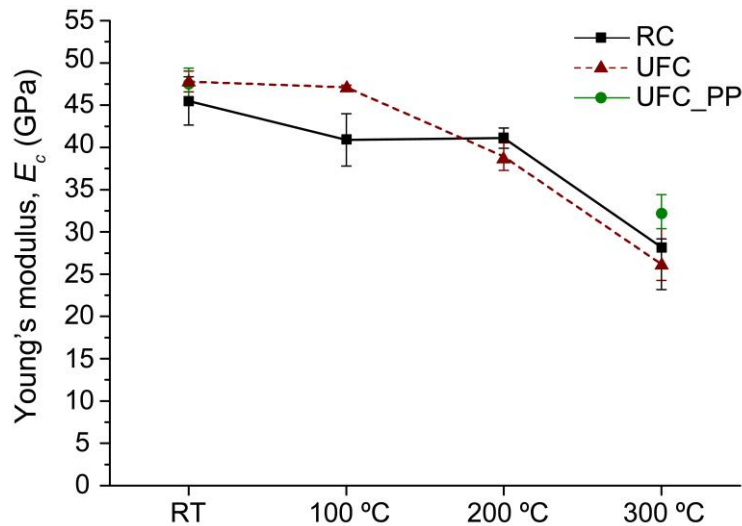
344

Figure 5: Compressive strength of all mixes at RT, 100 °C, 200 °C, and 300°C

345

346 **4.2.2 Young's modulus (E_c)**

347 At room temperature, Young's modulus was slightly higher in fibre-reinforced concrete (UFC
348 and UFC_PP). However, it cannot be concluded that the addition of fibres (at the rates used)
349 showed a clear influence, as observed by other authors [31,73]. At 100 °C, a 10% decrease was
350 observed in RC (plain concrete) due to the damage inflicted by the vapour pressure resulting
351 from moisture evaporation. However, this decrease was unnoticed in Young's modulus when
352 the matrix was reinforced exclusively with steel fibres (UFC), as shown by the results (Figure 6).
353 At 200 °C, a 20% and 19% decrease was observed in RC and UFC, respectively. Note that both
354 mixes (RC and UFC) showed a similar decrease in Young's modulus. Hence, steel-fibre
355 reinforcement does not exert a direct influence on this property [74]. At 300 °C, a 38%, 36%,
356 and 31% decrease was observed in RC, UFC, and UFC_PP, respectively. A mitigating effect of PP
357 fibres on the heating damage was noted. Although the highest Young's modulus values at 300
358 °C were those of concrete with PP fibres, they were still lower than those recorded at ambient
359 temperature.

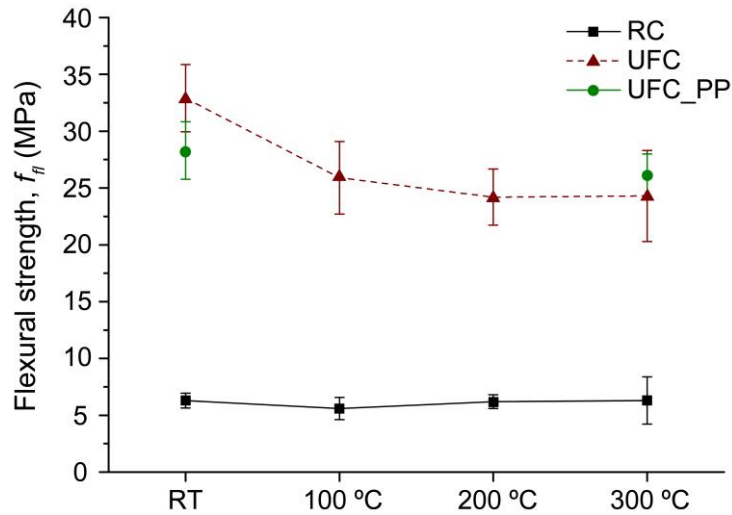


360
361 **Figure 6: Young's modulus of all mixes at RT, 100 °C, 200 °C, and 300°C**

362 **4.2.3 Flexural strength (f_{fl})**

363 At room temperature, flexural strength (f_{fl}) exhibited a remarkable enhancement in fibre-
364 reinforced mixes; it increased fivefold in the UFC and fourfold in the UFC_PP mix (Figure 7).
365 The growth of flexural strength was due to the crack bridging effect of steel fibres and the
366 decrease of entrapped air due to the presence of steel fibres in the concrete matrix (see Figure
367 3.a). At 100 °C, flexural strength decreased by 11% in RC and 21% in UFC due to effects similar
368 to those described on compressive strength. Note that the detrimental effect of heating
369 affected fibre-reinforced concrete more strongly in relative terms. In this mix, the evacuation
370 of vapour pressure is rarely effective because of its lower porosity (Figure 2). In 200 °C and 300
371 °C tests, the heating process led to spalling failure in some samples of plain concrete (RC); by
372 contrast, tests conducted in fibre-reinforced samples were apparently unaffected by spalling.
373 As observed, no significant changes were observed in the average values of flexural strength in

374 plain concrete (RC), although the standard deviation was much higher. A slight decrease was
 1 375 observed at 200 °C and 300 °C in UFC, showing that the strongest damaging effect on this
 2 376 property occurred when heating at 100 °C, in comparison with room temperature results. Note
 3 377 that spalling failure occurred in UFC at 300 °C and the standard deviation increased
 4 378 significantly as a result. The PP fibre-reinforced concrete (UFC_PP) exhibited an 8% decrease at
 5 379 300 °C and an unremarkable increase of standard deviation since spalling failure was not
 6 380 induced.



381
 382 **Figure 7: Flexural strength of mixes at RT, 100 °C, 200 °C, and 300 °C**

383 **4.2.4 Fracture energy (G_f)**

384 Table 5 shows the mean values of each fracture energy determined, as well as the standard
 385 deviation expressed as a percentage of the mean value. At room temperature, fracture energy
 386 enhanced significantly mainly due to the bridging effect of the steel fibres, which greatly
 387 increases the energy absorption capacity of fibre-reinforced concrete [75]. The highest average
 388 value was reached in steel fibre-reinforced concrete (UFC), because its lower porosity (Figure
 389 4) implied higher work-of-fracture, as shown by the higher flexural strength values in Figure 7.
 390 When the temperature increased (100 °C, 200 °C, and 300 °C), vapour pressure and
 391 dehydration generated internal damage which increased the number of pores, especially
 392 around 0.15 mm pore size (Figure 4), and decreased the fracture energy (Table 5). Note that
 393 the fracture energy value at 300 °C was higher with less deviation in PP fibre-reinforced
 394 concrete (UFC_PP). The reason why this happened despite the strength reduction due to
 395 melting of the PP fibres is that, as already explained, thermal damage (see Figure 4) caused by
 396 moisture evaporation and dehydration was mitigated because the high pressure was more
 397 easily evacuated.

401

Table 5: Fracture energy of mixes

Temperature	G_F (kN/m)		
	RC	UFC	UFC-PP
RT	0.061 (3%)	47.2 (5%)	40.7 (6%)
100 °C	-	32.7 (9%)	-
200 °C	-	28.7 (18%)	-
300 °C	-	22.5* (25%)	28.5 (12%)

402

* Spalling effect observed in some samples during the heating process.

403

In addition, the mean bilinear cohesive laws were determined for each concrete and temperature (Figure 8.a and b). The cohesive law parameters of each bilinear diagram are shown in Table 6. Note that the analysis of the bilinear cohesive diagrams provides disassociated information through the first and second linear branches. The first linear branch depends mainly on the micro-cracking process while the second one depends on frictional interlocking [76].

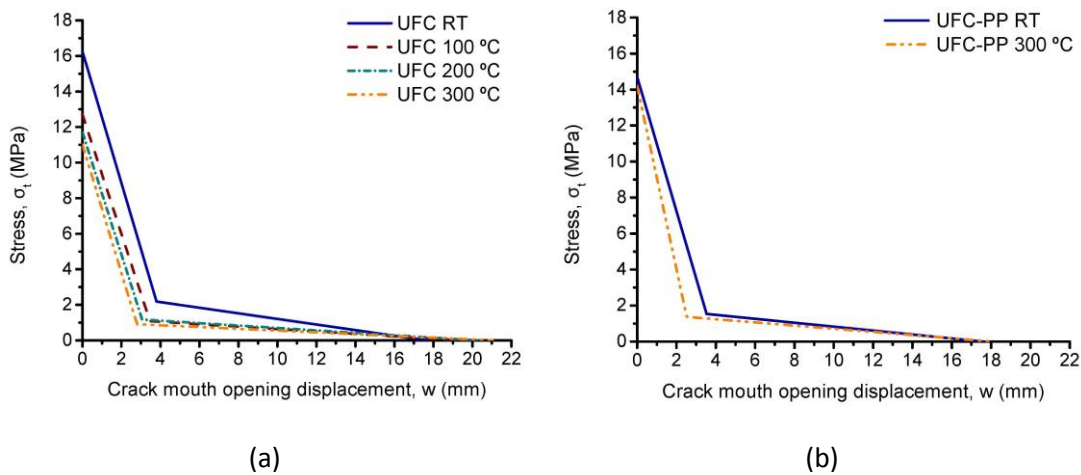
404

405

406

407

408



409

Figure 8: Bilinear cohesive law: UFC and UFC-PP

410

According to the results shown in Table 6, the initial fracture energy (G_f) represented essentially the main part of the fracture energy (G_F), with values ranging between 65%-74% of G_F . Hence, the energy to generate the micro-cracking of the matrix required three-fourths of the energy implied in the monotonic fracture process. The lowest values of initial fracture energy, in relative terms, were reached at higher temperatures. Less energy was required to generate micro-cracking because of the damage produced in the matrix (i.e., the presence of a more significant number of internal flaws). The initial fracture energy decreased by 53% from RT to 300 °C. The second linear branch and the displacement at failure decreased with heating up to 300 °C according to the fracture energy of the frictional interlocking ($G_F - G_f$). The thermal deterioration of the matrix caused a more predominant strain of the material. The higher deformation and the bridging effect of the steel fibres resulted in higher displacements at failure (w_u). The lower thermal degradation in concrete mixes with PP fibres (Figure 3.a) showed a similar trend to that of UFC, but with fewer significant effects in relative terms. The initial fracture energy of UFC-PP decreased by 32%. Additionally, the frictional interlocking

411

412

413

414

415

416

417

418

419

420

421

422

423

424 process was less remarkable in the fracture process of UFC-PP since UFC-PP maintained its
 425 fracture properties in a more uniform way with increasing temperature than UFC did.

426 **Table 6: Bilinear cohesive law parameters**

	UFC					UFC-PP				
	a_1 (mm ⁻¹)	a_2 (mm ⁻¹)	w_1 (mm)	w_u (mm)	G_f (kN/m)	a_1 (mm ⁻¹)	a_2 (mm ⁻¹)	w_1 (mm)	w_u (mm)	G_f (kN/m)
RT	3.71	0.16	4.37	17	35.4	3.73	0.11	3.94	17	28.9
100 °C	3.36	0.07	3.78	19	24.0	-	-	-	-	-
200 °C	3.44	0.07	3.40	20	19.9	-	-	-	-	-
300 °C	3.61	0.05	3.04	21	16.7	5.09	0.09	2.78	18	19.8

427

428 4.3 Fatigue behaviour

429 In this section, we analyse the experimental data obtained from the flexural fatigue tests of
 430 each mix (i.e., reference concrete, steel fibre-reinforced concrete, and steel-PP fibre-
 431 reinforced concrete). At least ten fatigue tests corresponding to several stress levels were
 432 taken into account in the evaluation to apply the probabilistic fatigue model [61].

433 Table 7 presents the results of the fatigue tests for the reference concrete, RC (plain concrete),
 434 at various stress levels and exposure to RT and 100 °C. Premature failure by spalling was
 435 observed during the heating process inside the furnace in some heated RC specimens at 200 °C
 436 and 300 °C. In those cases, few fatigue test data were available to run the probabilistic fatigue
 437 model [53], so they were not included in Table 7. Fatigue results exhibited a considerable
 438 scattering of more than two orders of magnitude, which is commonly accepted in the
 439 assessment of fatigue life in concrete [22,77], even at a particular stress level. This is
 440 essentially due to the heterogeneous composition of the concrete (i.e., cement paste,
 441 aggregates, fibres) and the statistical nature of the fatigue phenomenon [12].

442

443

444

445

446

Table 7: Stress level and fatigue life data for the reference concrete (RC)

RC-RT		RC-100 °C	
Stress level, S (MPa)	Fatigue life, N (cycles)	Stress level, S (MPa)	Fatigue life, N (cycles)
5.82	6	5.08	32
5.50	19	4.79	913
4.85	16,108	4.51	18
4.53	99	4.23	18,943
4.53	1,225	3.95	9,931
4.21	43,000	3.67	23,219
3.88	94	3.38	62,337
3.88	4,888	3.10	228,219
3.72	1,065	2.82	228,635
3.56	93,700	2.54	669,156
3.40	16	2.20	2,000,000*
3.24	2,000,000*	1.97	670,925
		1.69	2,000,000*

447

* run-out test

448 The fatigue data for the steel fibre-reinforced concrete mixes (UFC) are presented in Table 8.
 449 The tests were carried out for various stress levels at room temperature, 100 °C, and 200 °C. At
 450 300 °C, some of the specimens prematurely exploded by spalling, so insufficient data were
 451 available for the S-N field determination.

452

453

454

455

456

457

458

459

Table 8: Stress level and fatigue life data for the steel fibre-reinforced concrete (UFC)

UFC-RT		UFC-100 °C		UFC-200 °C	
Stress level, S (MPa)	Fatigue life, N (cycles)	Stress level, S (MPa)	Fatigue life, N (cycles)	Stress level, S (MPa)	Fatigue life, N (cycles)
29.66	79	23.39	394	21.82	126
28.01	2,150	22.09	2,597	21.82	9,579
26.36	631	22.09	42,027	21.82	44,714
25.54	33	22.09	64	21.82	55,939
24.71	3,998	20.79	4,513	20.60	5,914
23.89	15,836	20.79	230	20.00	34,155
23.07	5,030	20.14	2,120	19.39	20
22.24	16,911	19.49	7	19.39	18,396
21.42	83,875	18.97	168	18.18	46,977
20.59	33,790	18.19	272	17.57	16,656
19.77	256,282	17.41	928	16.97	44
18.12	423,098	17.41	7,649	15.76	2,688
16.48	2,000,000*	16.11	7,807	14.54	2,000,000*
		13.00	2,000,000*		

* run-out test

460

461 Table 9 summarises the fatigue results for the combination of steel and polypropylene fibre-
 462 reinforced concrete (UFC_PP). This mix was only tested at room temperature and 300 °C. No
 463 spalling effects were observed in this mix during the heating process, since the addition of PP
 464 fibres reduced the thermal damage caused by high pore pressure and dehydration in the
 465 matrix, as explained in detail in subsection 4.1.

466

467

468

469

470 **Table 9: Stress level and fatigue life data for the PP and steel fibre-reinforced concrete**
 471 **(UFC_PP)**

UFC_PP-RT		UFC_PP-300 °C	
Stress level, S (MPa)	Fatigue life, N (cycles)	Stress level, S (MPa)	Fatigue life, N (cycles)
25.47	101	23.40	3,252
24.20	26,552	22.75	2,339
24.06	23,746	22.10	45,560
23.35	15	22.100	11,135
22.96	28	21.45	13,780
22.64	71,921	20.80	2,595
21.93	38,209	20.15	14,623
21.23	64,187	19.50	66,212
20.87	40,791	18.85	3,773
20.52	64	18.20	139
19.81	2,299	17.86	67,319
19.10	1,617,740	17.55	58,000
18.40	1,617,740	16.90	2,000,000*
17.69	2,000,000*		

* run-out test

472

473 Table 10 shows the model parameters estimated from the experimental fatigue tests
 474 according to the probabilistic fatigue model developed by Castillo and Fernández-Canteli [53].
 475 The fatigue model is based on the compatibility condition between distributions P(GP;N) and
 476 P(N;GP). It depends on five parameters: exp(C) is the horizontal asymptote which represents
 477 the endurance limit; exp(B) is the vertical asymptote; λ , δ , and β are the location, scale and
 478 shape parameters, respectively, of the Weibull distribution, where λ defines the position of the
 479 zero-percentile curve in the probabilistic assessment of the S-N field.

480

481

482

483 **Table 10: Model parameters estimated according to the probabilistic fatigue model [61]**

	β	B	C	δ	λ
RC-RT	1.01	6.90	1.16	0.54	0.01
RC-100 °C	1.31	2.86	0.70	3.56	0.00
UFC-RT*	1.86	0.00	2.30	1.04	6.97
UFC-100 °C*	1.40	4.12	2.46	1.84	0.00
UFC-200 °C	1.01	2.97	2.38	1.35	0.02
UFC_PP-RT	1.87	7.66	2.74	0.96	0.00
UFC_PP-300 °C	1.41	4.89	2.81	0.88	0.00

484

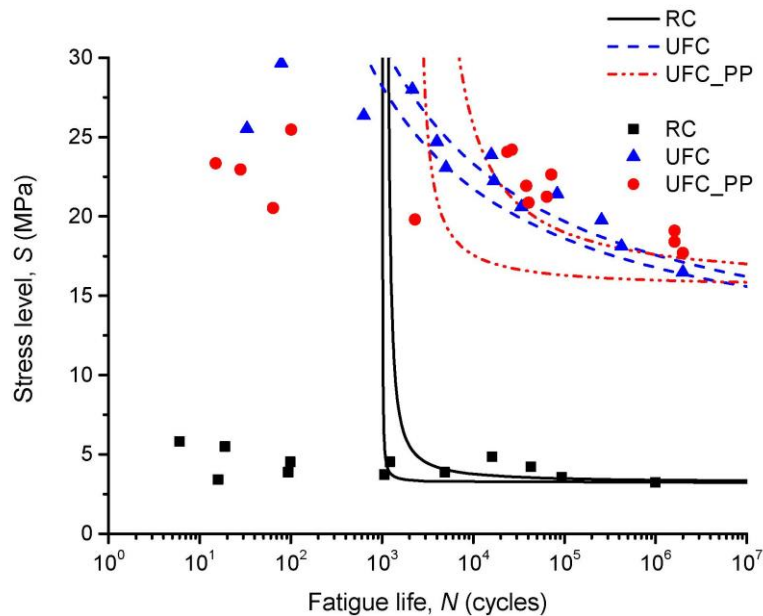
485 The model fit the experimental fatigue data. However, in the graphical representation of the
 486 results, both low-cycle fatigue and long-cycle fatigue breaks could occur simultaneously in the
 487 upper level ($S=0.9f_{fl}$). This fact is evidenced by the convex curvature of the upper levels and by
 488 the coincidence of pseudo-static breaks and fatigue breaks for the same stress level. The
 489 model developed by Castillo and Fernández-Canteli assumes that the damage mechanism is
 490 the same for all stress levels. Thus, the results of the higher level should not be used in the
 491 analysis to fit the model for concrete. A more thorough analysis could even rule out the 90%
 492 stress level. In this study, stress levels higher than 80% ($S>0.8f_{fl}$) were not considered to
 493 determine the S-N curves. Additionally, in the interest of clarity, only the 0.05 and 0.50
 494 percentile curves for each concrete mix and temperature tested were plotted with the
 495 experimental fatigue data.

496 **4.3.1 Influence of the fibres on fatigue life**

497 For the purpose of examining the influence of fibres on the fatigue behaviour of the concrete
 498 mixes manufactured, the S-N field for each concrete was determined by applying the
 499 probabilistic fatigue model described in subsection 3.2 [61].

500 The fatigue crack growth in the concretes tested showed three stages: initial growth, steady-
 501 state growth, and final accelerated growth [15,78]. The initial crack length, generated by the
 502 first load application, was prominent in fibre-reinforced concrete because the concrete was
 503 loaded above the first cracking strength (i.e., the concrete matrix strength). This effect was
 504 more noticeable when the concrete had a greater number of steel fibres since the difference
 505 between the first cracking and ultimate strength increased. Furthermore, because of the high
 506 number of fibres, crack propagation happened in a fairly steady way throughout the fatigue
 507 process before ultimate failure occurred because of significant multiple cracking processes
 508 [15].

509 Figure 9 represents the 0.05 and 0.50 percentile curves for the reference concrete (RC), steel
 510 fibre-reinforced concrete (UFC), and steel-PP fibre-reinforced concrete (UFC_PP) at room
 511 temperature, respectively. The addition of steel fibres (UFC) in high amounts (2.5% in this
 512 research) led to higher stress levels at low load cycles compared to those of the reference
 513 concrete (Figure 9). In this case, the final failure was essentially due to the pull-out of the
 514 fibres [79]. The maximum stress level applied was remarkably close to the value of the
 515 ultimate monotonic flexural strength (Figure 7). As a result, micro-cracking and crack
 516 coalescence was quickly generated, consuming a prominent part of the initial fracture energy
 517 (Table 6) in each cycle. Accordingly, the concrete became severely cracked while the flexural
 518 stresses were predominantly strengthened by steel fibres. Under a high-cycle fatigue regime, a
 519 progressive weakening of the fibre-matrix interlocking was generated at lower load levels
 520 through steady micro-cracking. Thus, the efficiency of the bridging effect of fibres decreased,
 521 resulting in a similar endurance limit to that of UFC_PP (15.5 MPa, UFC, and 15.8 MPa, UFC_PP
 522 respectively), as observed in Figure 9. The addition of high-content steel fibres exerted a
 523 twofold beneficial effect on fatigue behaviour. On the one hand, its presence reduced total
 524 porosity and pore size (Figure 3.a), so the scattering of fatigue life was reduced because there
 525 were less internal flaws, as seen from the proximity of the 0.05 and 0.50 curves in Figure 8. On
 526 the other hand, greater stress levels were reached in low cycles. In steel-PP fibre-reinforced
 527 concrete (UFC_PP), the presence of the largest pores up to 4.6 mm in diameter (Figure 3.a)
 528 generated a higher stress concentration [80], thus requiring a lower fracture energy (Table 6).
 529 This led to lower fatigue life at high stress levels compared to the UFC case. Additionally, the
 530 larger range of pore sizes combined with their arbitrary generation in the microstructure led to
 531 a higher scattering in the fatigue life results, as observed from the separation of the 0.05 and
 532 0.50 percentile curves of UFC_PP in Figure 9.

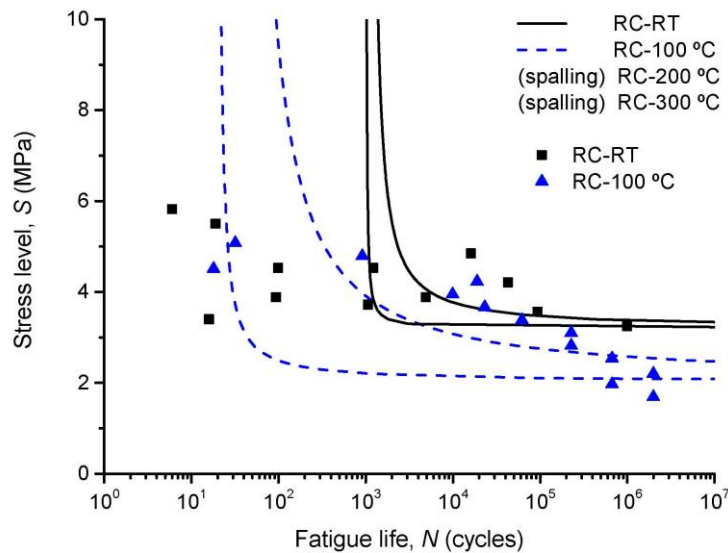


533
 534 **Figure 9: S-N curves for each mix at room temperature**
 535

536 **4.3.2 Influence of temperature on fatigue life**

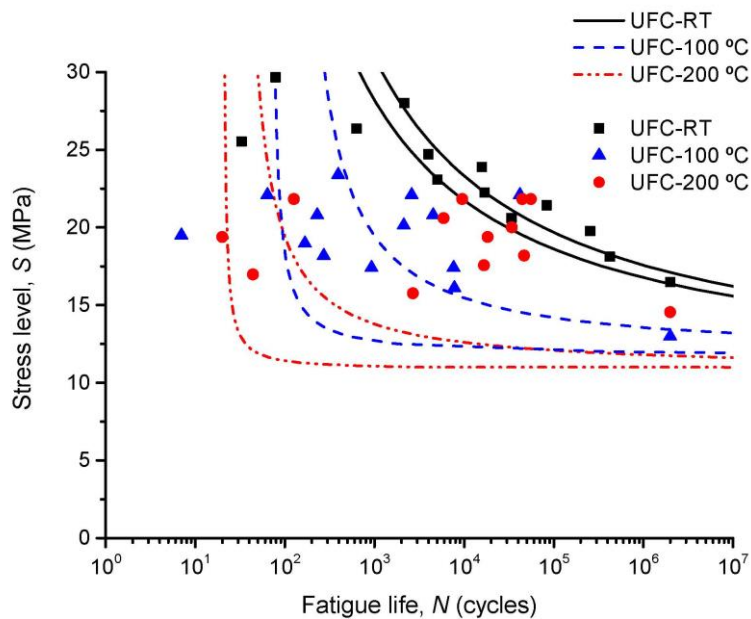
537 Figure 10 represents the influence of temperature on the S-N field for the reference concrete
 538 (RC) exposed to room temperature and 100 °C. As failure by spalling was observed in some
 539 heated RC specimens at 200 °C and 300 °C, an insufficient number of fatigue tests were
 540 available for the application of the probabilistic fatigue model [53]. Hence, only the S-N curves
 541 of the RC mix at room temperature and 100 °C are presented in Figure 10.

542 At room temperature, the endurance limit was reached at a stress level of 3.3 MPa (Figure 10).
 543 Heating to 100 °C led to the generation of microcracks in the concrete matrix, induced by the
 544 high pore pressure because of capillary pressure and partial dehydration [48]. This resulted in
 545 a more cracked matrix, which implied a significant decrease of the endurance limit (by 32%)
 546 from approximately 3.3 MPa at RT to 2.1 MPa at 100 °C (Figure 10). This thermal damage by
 547 heating was consistent with the decrease of monotonic flexural strength observed in Figure 7.
 548 Furthermore, repeated loading under maximum monotonic strength led to the creation and
 549 growth of micro-defects (e.g., pores, microcracks) following the minimum energy path.
 550 Heating promoted a progressive degeneration of the internal structure which resulted in the
 551 decrease of material strength, as observed in the monotonic flexural results (Figure 7). At 100
 552 °C, the matrix was initially more degraded due to thermal damage. Thus, the deleterious crack
 553 propagation by fatigue loading was more effective and led to a significant decrease of stress
 554 levels, which did not make it possible to clearly define the endurance limit (see Figure 10). As
 555 mentioned in section 4.1, the damage generated by the temperature did not affect all pore
 556 sizes equally. Moreover, the uneven heating between the external and internal areas of the
 557 specimen caused more arbitrary damage. As a result, fatigue life results were more scattered,
 558 as can be seen from the 0.05 and 0.50 percentile curves of RC-100 °C in Figure 9.



559
 560 **Figure 10: S-N curves for the reference concrete (RC) at different temperatures**
 561

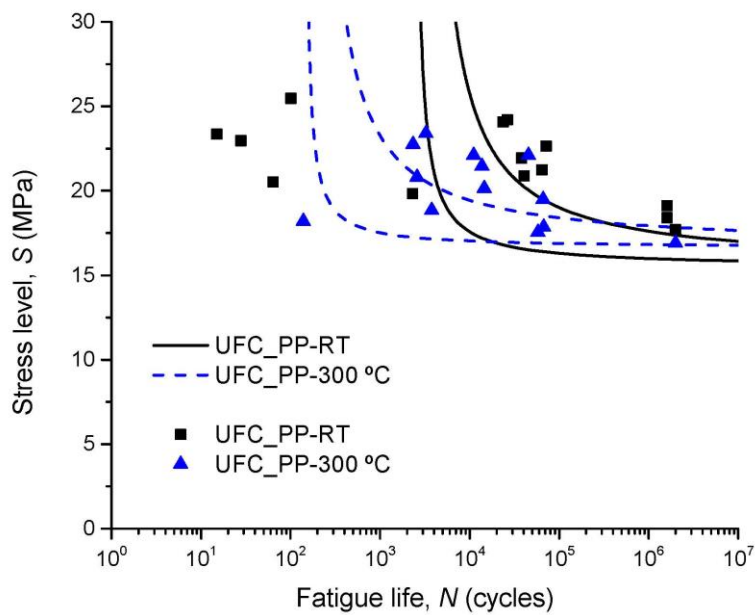
562 In steel fibre-reinforced concrete (UFC) at room temperature (Figure 11), the endurance limit
 563 was reached at a stress level of 15.5 MPa. In addition, low scattering was observed in the
 564 separation band between the 0.05 and 0.50 percentile curves. The low scattering was due to
 565 the lower total porosity and, particularly, to the narrow pore-size range observed (Figure 3.a).
 566 In heated tests, the concrete matrix underwent internal degradation during the heating
 567 process (high pore pressure and dehydration) at 100 °C and 200 °C. Yet, the fatigue limit values
 568 achieved were slightly lower than those at room temperature (12 MPa and 10.8 MPa of stress
 569 level at 100 °C and 200 °C, respectively). This demonstrates how the sewing effect of steel
 570 fibres progressively weakened at low load levels. At high load levels, the generation of micro-
 571 defects due to thermal gradients in the concrete matrix was initially higher at 100 °C and even
 572 greater at 200 °C. As a result, the fracture energy required up to failure was lower, as observed
 573 in Table 5. Since the maximum stress applied represented a predominant part of the ultimate
 574 flexural strength, crack growth was more significant in each cycle and a higher part of the
 575 initial fracture energy was therefore consumed. Hence, the concrete with the lowest initial
 576 fracture energy (UFC at 200 °C) exhibited lower fatigue life at higher load levels (Figure 10). It is
 577 worth noting that, because thermal gradients are randomly distributed, the defects induced by
 578 thermal damage are also randomly generated in the matrix [22]. This resulted in higher
 579 scattering of the mechanical (Figure 7) and fracture properties (Table 5) and fatigue behaviour
 580 (Figure 11). The separation between the 0.05 and 0.50 percentile curves of UFC-100 °C and
 581 UFC-200 °C (Figure 11) greater in comparison with the other types of concrete, evidencing
 582 higher scattering between fatigue life results (Table 8).



583
 584 **Figure 11: S-N curves for steel fibre-reinforced concrete (UFC) at different temperatures**

585 For the steel and polypropylene fibre-reinforced concrete mix (UFC_PP), the endurance limit at
 586 room temperature represented a stress level of 15.9 MPa. The addition of PP fibres increased
 587 the total porosity of the matrix and the pore-size range. The presence of larger pores
 588 decreased fatigue life at high load levels according to the lower monotonic flexural strength

589 (Figure 7) and fracture energy (Table 5 and 6). At 300 °C, the thermal degradation of this
 590 concrete was generated by two stages: the evaporation of moisture and capillary pores
 591 between 20 °C and 250 °C, and the dehydration of the C-S-H gel in the range of 250 °C to 400
 592 °C [48]. The presence of PP fibres and their partial melting at 160 °C prevented the UFC_PP
 593 from failing by spalling during the heating process inside the furnace. The better evacuation of
 594 high pore pressure by the capillary pores and dehydration due to the generation of a network
 595 of channels by the melting of the PP fibres around 160 °C [44] led to a less degraded matrix. As
 596 observed, the lower range of pore-size distribution at 300 °C was almost invariant compared to
 597 room temperature. This led to a reduction of initial fracture energy by approximately 30%
 598 compared to the RT results. Consequently, the S-N field of UFC_PP at 300 °C showed a similar
 599 endurance limit to that of UFC_PP at room temperature (i.e., 15.9 MPa at RT and 16.7 MPa at
 600 300 °C). Additionally, the similar pore size distribution led to lower scattering between the
 601 results represented by the 0.05 and 0.50 percentile curves (Figure 12). This effect was
 602 consistent in relative terms with that observed in the results regarding mechanical (Figure 5, 6
 603 and 7) and fracture properties (Table 5).



604
 605 **Figure 12: S-N curves for the PP and steel fibre-reinforced concrete (UFC_PP) at different**
 606 **temperatures**

607 **5. Conclusions**

608 The following conclusions can be drawn from the results:

- 609 • The probabilistic fatigue model used fit the experimental fatigue data. However, the model
 610 assumed the damage mechanism was the same for all stress levels. In fact, this mechanism
 611 differed for fibre-reinforced concrete, in which the effectiveness of the fibre-concrete

612 interlock played an essential role in crack propagation. For this reason, stress levels closest
613 to static strength should not be used in the analysis.

614 • The addition of steel fibres resulted in a more significant high endurance limit (78%)
615 compared to plain concrete. Moreover, the inherent scattering of the concrete decreased
616 since the mere presence of the fibres reduced the porosity of the matrix and gave it a
617 more stable strengthening behaviour.

618 • The addition of polypropylene fibres to the mix with steel fibres did not significantly affect
619 the endurance limit, although the presence of larger pores in the matrix increased.
620 However, this change in the matrix did produce a significant higher scattering in fatigue
621 behaviour.

622 • The heating of plain concrete increased total porosity, which significantly affected the
623 scattering of the S-N field. As the increase of porosity was not significant in relative terms,
624 the endurance limit was slightly reduced.

625 • In relative terms, the temperature effect at 100 °C and 200 °C increased the porosity of the
626 steel fibre-reinforced concrete more significantly and reduced its endurance limit (22.5
627 and 30.3%, respectively). In addition, the arbitrary distribution of damage generated a
628 more random S-N field.

629 • The increase in the number of pores due to thermal degradation at 300 °C in the steel-
630 polypropylene fibre-reinforced concrete did not show significant effects on the endurance
631 limit or the S-N field scatter. Thus, fatigue behaviour was remarkably the most stable at
632 any temperature.

633 **Acknowledgments**

634 The authors acknowledge the financial support provided to this study by the Spanish Ministry
635 of the Economy and Competitiveness under projects number BIA2016-75431-R and PID2019-
636 110928RB-C33.

637 **References**

638 [1] Xiao J, Li H, Yang Z. Fatigue behavior of recycled aggregate concrete under compression
639 and bending cyclic loadings. *Construction and Building Materials* 2013;38:681–8.
640 doi:10.1016/j.conbuildmat.2012.09.024.

641 [2] Bennet EW. Fatigue of plain concrete in compression under varying sequences of two-
642 level programme loading. *International Journal of Fatigue* 1980;2:171–5.
643 doi:10.1016/0142-1123(80)90045-6.

1
2
3
4
5
6
7
8
9
10
11
12
13
14
15
16
17
18
19
20
21
22
23
24
25
26
27
28
29
30
31
32
33
34
35
36
37
38
39
40
41
42
43
44
45
46
47
48
49
50
51
52
53
54
55
56
57
58
59
60
61
62
63
64
65

644 [3] Plizzari GA, Cangiano S, Alleruzzo S. The fatigue behaviour of cracked concrete. *Fatigue & Fracture of Engineering Materials & Structures* 2007;20:1195–206. doi:10.1111/j.1460-2695.1997.tb00323.x.

647 [4] Kaur G, Singh SP, Kaushik SK. Fatigue analysis of fibrous concrete with cement additions. *Proceedings of the ICE - Construction Materials* 2014;167:79–90. doi:10.1680/coma.12.00014.

650 [5] Zhang B, Phillips DV, Wu K. Effect of Loading Frequency and Stress Reversal on Fatigue Life of Plain Concrete. *Magazine of Concrete Research* 1996;48:361–75. doi:10.1680/mac.1996.48.177.361.

653 [6] Raithby KD. Flexural Fatigue Behaviour of Plain Concrete. *Fatigue of Engineering Materials and Structures* 1979;2:269–78. doi:10.1111/j.1460-2695.1979.tb01085.x.

655 [7] Shi XP, Fwa TF, Tan SA. Flexural Fatigue Strength of Plain Concrete. *ACI Materials Journal* 1993;90:435–40. doi:10.14359/3872.

657 [8] Kesler C. Effect of speed of testing on flexural strength of concrete. *Proceedings of the Thirty-Second Annual Meeting of the Highway Research Board* 1953;32:251–8.

659 [9] Kolluru S V, O’Neil EF, Popovics JS, Shah SP. Crack propagation in flexural fatigue of concrete. *Journal of Engineering Mechanics, ASCE* 2000;126:891–8. doi:10.1061/(ASCE)0733-9399(2000)126:9(891).

662 [10] Johnston CD, Zemp RW. Flexural Fatigue Performance of Steel Fibre Reinforced Concrete. Influence of Fibre Content, Aspect Ratio and Type. *ACI Materials Journal* 1991;88:374–83. doi:10.14359/1875.

665 [11] Morris AD, Garrett GG. A comparative study of the static and fatigue behaviour of plain and steel fibre reinforced mortar in compression and direct tension. *The International Journal of Cement Composites and Lightweight Concrete* 1981;3:73–91. doi:10.1016/0262-5075(81)90002-6.

669 [12] Goel S, Singh SP. Fatigue performance of plain and steel fibre reinforced self compacting concrete using S–N relationship. *Engineering Structures* 2014;74:65–73. doi:10.1016/j.engstruct.2014.05.010.

1
2
3
4
5
6
7
8
9
10
11
12
13
14
15
16
17
18
19
20
21
22
23
24
25
26
27
28
29
30
31
32
33
34
35
36
37
38
39
40
41
42
43
44
45
46
47
48
49
50
51
52
53
54
55
56
57
58
59
60
61
62
63
64
65

672 [13] Singh SP, Kaushik SK. Fatigue strength of steel fibre reinforced concrete in flexure.
673 Cement and Concrete Composites 2003;25:779–86. doi:10.1016/S0958-9465(02)00102-
674 6.

675 [14] Lee MK, Barr BIG. An overview of the fatigue behaviour of plain and fibre reinforced
676 concrete. Cement and Concrete Composites 2004;26:299–305. doi:10.1016/S0958-
677 9465(02)00139-7.

678 [15] Matsumoto T, Li VC. Fatigue life analysis of fiber reinforced concrete with a fracture
679 mechanics based model. Cement and Concrete Composites 1999;21:249–61.
680 doi:10.1016/S0958-9465(99)00004-9.

681 [16] Zhang J, Stang H, Li VC. Fatigue life prediction of fiber reinforced concrete under
682 flexural load. International Journal of Fatigue 1999;21:1033–49. doi:10.1016/S0142-
683 1123(99)00093-6.

684 [17] Goel S, Singh SP, Singh P. Fatigue Analysis of Plain and Fiber-Reinforced Self-
685 Consolidating Concrete. ACI Materials Journal 2012;109:573–82.
686 doi:10.14359/51684089.

687 [18] Lappa ES. PhD. Thesis: High Strength Fibre Reinforced Concrete: Static and fatigue
688 behaviour in bending. 2007.

689 [19] Oneschkow N. Fatigue behaviour of high-strength concrete with respect to strain and
690 stiffness. International Journal of Fatigue 2016;87:38–49.
691 doi:10.1016/j.ijfatigue.2016.01.008.

692 [20] Kim J-K, Kim Y-Y. Experimental study of the fatigue behavior of high strength concrete.
693 Cement and Concrete Research 1996;26:1513–23. doi:10.1016/0008-8846(96)00151-2.

694 [21] Hop T. Fatigue of High Strength Concrete. Building Science 1968;3:65–80.
695 doi:10.1016/0007-3628(68)90017-0.

696 [22] Vicente MA, González DC, Mínguez J, Tarifa MA, Ruiz G, Hindi R. Influence of the pore
697 morphology of high strength concrete on its fatigue life. International Journal of Fatigue
698 2018;112:106–16. doi:10.1016/j.ijfatigue.2018.03.006.

1
2
3
4
5
6
7
8
9
10
11
12
13
14
15
16
17
18
19
20
21
22
23
24
25
26
27
28
29
30
31
32
33
34
35
36
37
38
39
40
41
42
43
44
45
46
47
48
49
50
51
52
53
54
55
56
57
58
59
60
61
62
63
64
65

699 [23] Petkovic G, Lenschow R, Stemland H, Rosseland S. Fatigue of high-strength concrete.
700 ACI Symposium Publication 1990;121:505–26. doi:10.14359/3740.

701 [24] Singh SP, Mohammadi Y, Kaushik SK. Flexural Fatigue Analysis of Steel Fibrous Concrete
702 Containing Mixed Fibers. ACI Materials Journal 2005;102:438–44. doi:10.14359/14807.

703 [25] Al-Azzawi BS, Karihaloo BL. Flexural fatigue behavior of a self-compacting ultrahigh
704 performance fiber-reinforced concrete. Journal of Materials in Civil Engineering
705 2017;29:04017210. doi:10.1061/(ASCE)MT.1943-5533.0002051.

706 [26] Cachim PB, Figueiras JA, Pereira PAA. Fatigue behavior of fiber-reinforced concrete in
707 compression. Cement and Concrete Composites 2002;24:211–7. doi:10.1016/S0958-
708 9465(01)00019-1.

709 [27] Nicolaidis D, Kanellopoulos A, Karihaloo BL. Fatigue life and self-induced volumetric
710 changes of CARDIFRC. Magazine of Concrete Research 2010;62:679–83.
711 doi:10.1680/mac.9.00149.

712 [28] Farhat FA, Nicolaidis D, Kanellopoulos A, Karihaloo BL. High performance fibre-
713 reinforced cementitious composite (CARDIFRC) - Performance and application to
714 retrofitting. Engineering Fracture Mechanics 2007;74:151–67.
715 doi:10.1016/j.engfracmech.2006.01.023.

716 [29] Wang X, Yu R, Song Q, Shui Z, Liu Z, Wu S, et al. Optimized design of ultra-high
717 performance concrete (UHPC) with a high wet packing density. Cement and Concrete
718 Research 2019;126:105921. doi:10.1016/j.cemconres.2019.105921.

719 [30] Yu R, Spiesz P, Brouwers HJH. Mix design and properties assessment of Ultra-High
720 Performance Fibre Reinforced Concrete (UHPRFC). Cement and Concrete Research
721 2014;56:29–39. doi:10.1016/j.cemconres.2013.11.002.

722 [31] Ríos JD, Leiva C, Ariza MP, Seidl S, Cifuentes H. Analysis of the tensile fracture properties
723 of ultra-high-strength fiber-reinforced concrete with different types of steel fibers by X-
724 ray tomography. Materials & Design 2019:107582. doi:10.1016/j.matdes.2019.107582.

725 [32] Song Q, Yu R, Wang X, Rao S, Shui Z. A novel Self-Compacting Ultra-High Performance
726 Fibre Reinforced Concrete (SCUHPFRC) derived from compounded high-active powders.

1
2
3
4
5
6
7
8
9
10
11
12
13
14
15
16
17
18
19
20
21
22
23
24
25
26
27
28
29
30
31
32
33
34
35
36
37
38
39
40
41
42
43
44
45
46
47
48
49
50
51
52
53
54
55
56
57
58
59
60
61
62
63
64
65

727 Construction and Building Materials 2018;158:883–93.
728 doi:10.1016/j.conbuildmat.2017.10.059.

729 [33] Yousefieh N, Joshaghani A, Hajibandeh E, Shekarchi M. Influence of fibers on drying
730 shrinkage in restrained concrete. Construction and Building Materials 2017;148:833–45.
731 doi:10.1016/j.conbuildmat.2017.05.093.

732 [34] Cao M, Zhang C, Lv H. Mechanical response and shrinkage performance of cementitious
733 composites with a new fiber hybridization. Construction and Building Materials
734 2014;57:45–52. doi:10.1016/j.conbuildmat.2014.01.088.

735 [35] Makita T, Brühwiler E. Tensile fatigue behaviour of ultra-high performance fibre
736 reinforced concrete (UHPFRC). Materials and Structures 2014;47:475–91.
737 doi:10.1617/s11527-013-0073-x.

738 [36] Tran NT, Tran TK, Jeon JK, Park JK, Kim DJ. Fracture energy of ultra-high-performance
739 fiber-reinforced concrete at high strain rates. Cement and Concrete Research
740 2016;79:169–84. doi:10.1016/j.cemconres.2015.09.011.

741 [37] Yoo DY, Banthia N. Mechanical properties of ultra-high-performance fiber-reinforced
742 concrete: A review. Cement and Concrete Composites 2016;73:267–80.
743 doi:10.1016/j.cemconcomp.2016.08.001.

744 [38] Yoo DY, Kim S, Park GJ, Park JJ, Kim SW. Effects of fiber shape, aspect ratio, and volume
745 fraction on flexural behavior of ultra-high-performance fiber-reinforced cement
746 composites. Composite Structures 2017;174:375–88.
747 doi:10.1016/j.compstruct.2017.04.069.

748 [39] Alonso MC, Vera-Agullo J, Guerreiro L, Flor-Laguna V, Sanchez M, Collares-Pereira M.
749 Calcium aluminate based cement for concrete to be used as thermal energy storage in
750 solar thermal electricity plants. Cement and Concrete Research 2016;82:74–86.
751 doi:10.1016/j.cemconres.2015.12.013.

752 [40] Gil A, Medrano M, Martorell I, Lázaro A, Doblado P, Zalba B, et al. State of the art on
753 high temperature thermal energy storage for power generation . Part 1 — Concepts,

- 754 materials and modellization. *Renewable and Sustainable Energy Reviews* 2010;14:31–
1 755 55. doi:10.1016/j.rser.2009.07.035.
2
3
4 756 [41] Laing D, Steinmann WD, Tamme R, Richter C. Solid media thermal storage for parabolic
5 757 trough power plants. *Solar Energy* 2006;80:1283–9. doi:10.1016/j.solener.2006.06.003.
6
7
8
9 758 [42] Eidan J, Rasoolan I, Rezaeian A, Poorveis D. Residual mechanical properties of
10 759 polypropylene fiber-reinforced concrete after heating. *Construction and Building*
11 760 *Materials* 2019;198:195–206. doi:10.1016/j.conbuildmat.2018.11.209.
12
13
14
15
16 761 [43] Zhang B, Bicanic N. Fracture energy of high-performance concrete at high temperatures
17 762 up to 450°C: the effects of heating temperatures and testing conditions (hot and cold).
18 763 *Magazine of Concrete Research* 2006;58:277–88. doi:10.1680/macr.2006.58.5.277.
19
20
21
22 764 [44] Ríos JD, Cifuentes H, Leiva C, García C, Alba MD. Behavior of High-Strength
23 765 Polypropylene Fiber-Reinforced Self-Compacting Concrete Exposed to High
24 766 Temperatures. *Journal of Materials and Civil Engineering, ASCE* 2018;30:04018271.
25 767 doi:10.1061/(ASCE)MT.1943-5533.0002491.
26
27
28
29
30
31 768 [45] Cifuentes H, García F, Maeso O, Medina F. Influence of the properties of polypropylene
32 769 fibres on the fracture behaviour of low-, normal- and high-strength FRC. *Construction*
33 770 *and Building Materials* 2013;45:130–7. doi:10.1016/j.conbuildmat.2013.03.098.
34
35
36
37 771 [46] Bei S, Zhixiang L. Investigation on spalling resistance of ultra-high-strength concrete
38 772 under rapid heating and rapid cooling. *Case Studies in Construction Materials*
39 773 *2016;4:146–53. doi:10.1016/j.cscm.2016.04.001.*
40
41
42
43
44 774 [47] Kalifa P, Menneteau F-D, Quenard D. Spalling and pore pressure in HPC at high
45 775 temperatures. *Cement and Concrete Research* 2000;30:1915–27. doi:10.1016/S0008-
46 776 8846(00)00384-7.
47
48
49
50 777 [48] Ríos JD, Cifuentes H, Leiva C, Seidl S. Analysis of the mechanical and fracture behavior of
51 778 heated ultra-high-performance fiber-reinforced concrete by X-ray computed
52 779 tomography. *Cement and Concrete Research* 2019;119:77–88.
53 780 doi:10.1016/j.cemconres.2019.02.015.
54
55
56
57
58
59
60
61
62
63
64
65

1
2
3
4
5
6
7
8
9
10
11
12
13
14
15
16
17
18
19
20
21
22
23
24
25
26
27
28
29
30
31
32
33
34
35
36
37
38
39
40
41
42
43
44
45
46
47
48
49
50
51
52
53
54
55
56
57
58
59
60
61
62
63
64
65

781 [49] Cifuentes H, Karihaloo BL. Analysis of the early-age cracking in concrete made from
782 rapid hardening cement. *Hormigón Y Acero* 2018;69:101–12.
783 doi:10.1016/j.hya.2018.02.002.

784 [50] Chan SYN, Peng G, Chan JKW. Comparison between high strength concrete and normal
785 strength concrete subjected to high temperature. *Materials and Structures*
786 1996;29:616–9. doi:10.1007/BF02485969.

787 [51] Makita T, Brühwiler E. Tensile fatigue behaviour of Ultra-High Performance Fibre
788 Reinforced Concrete combined with steel rebars (R-UHPFRC). *International Journal of*
789 *Fatigue* 2014;59:145–52. doi:10.1016/j.ijfatigue.2013.09.004.

790 [52] Castillo E, Fernández-Canteli A, Koller R, Ruiz-Ripoll ML, García A. A statistical fatigue
791 model covering the tension and compression Wöhler fields. *Probabilistic Engineering*
792 *Mechanics* 2009;24:199–209. doi:10.1016/j.probengmech.2008.06.003.

793 [53] Fernández-Canteli A, Przybilla C, Nogal M, Aenlle ML, Castillo E. ProFatigue: A software
794 program for probabilistic assessment of experimental fatigue data sets. *Procedia*
795 *Engineering* 2014;74:236–41. doi:10.1016/j.proeng.2014.06.255.

796 [54] Deeb R, Ghanbari A, Karihaloo BL. Development of self-compacting high and ultra high
797 performance concretes with and without steel fibres. *Cement and Concrete Composites*
798 2012;34:185–90. doi:10.1016/j.cemconcomp.2011.11.001.

799 [55] Ríos JD, Mínguez J, Martínez-De La Concha A, Vicente MÁ, Cifuentes H. Microstructural
800 analyses of the addition of PP fibres on the fracture properties of high-strength self-
801 compacting concrete by X-ray computed tomography. *Construction and Building*
802 *Materials* 2020;261:14–7. doi:10.1016/j.conbuildmat.2020.120499.

803 [56] Ríos JD, Cifuentes H, Leiva C, Ariza MP, Ortiz M. Effect of polypropylene fibers on the
804 fracture behavior of heated ultra-high performance concrete. *International Journal of*
805 *Fracture* 2020;223:173–87. doi:10.1007/s10704-019-00407-4.

806 [57] Mazanec O, Lowke D, Schiel P. Mixing of high performance concrete: Effect of concrete
807 composition and mixing intensity on mixing time. *Materials and Structures/Materiaux*
808 *et Constructions* 2010;43:357–65. doi:10.1617/s11527-009-9494-y.

1
2
3
4
5
6
7
8
9
10
11
12
13
14
15
16
17
18
19
20
21
22
23
24
25
26
27
28
29
30
31
32
33
34
35
36
37
38
39
40
41
42
43
44
45
46
47
48
49
50
51
52
53
54
55
56
57
58
59
60
61
62
63
64
65

809 [58] EN-12390-3: 2009. Testing hardened concrete Part 3: Compressive strength of test
810 specimens, AENOR,. Brussels, European Committee for Standarization (CEN): 2009.

811 [59] EN-12390-13: 2014. Testing hardenes concrete Part 13: Determination of secant
812 modulus of elasticity in compression, AENOR,. Brussels, European Committee for
813 Standarization (CEN): 2014.

814 [60] RILEM TCM-85, Determination of the fracture energy of mortar and concrete by means
815 of three-point bend tests on notched beams. *Materials and Structures* 1985;18:287–90.
816 doi:10.1007/BF02472918.

817 [61] Castillo E, Fernández-Canteli A. *A Unified Statistical Methodology for Modeling Fatigue*
818 *Damage*. Springer Science & Business Media. ISBN: 978-978-1-4020-9182-7; 2009.

819 [62] Suescum-Morales D, Ríos JD, Martínez-De La Concha A, Cifuentes H, Jiménez JR,
820 Fernández JM. Cement and Concrete Research Effect of moderate temperatures on
821 compressive strength of ultra-high-performance concrete : A microstructural analysis
822 2021;140. doi:10.1016/j.cemconres.2020.106303.

823 [63] Peng GF, Niu XJ, Shang YJ, Zhang DP, Chen XW, Ding H. Combined curing as a novel
824 approach to improve resistance of ultra-high performance concrete to explosive
825 spalling under high temperature and its mechanical properties. *Cement and Concrete*
826 *Research* 2018;109:147–58. doi:10.1016/j.cemconres.2018.04.011.

827 [64] Wang R, Gao X, Zhang J, Han G. Spatial distribution of steel fibers and air bubbles in
828 UHPC cylinder determined by X-ray CT method. *Construction and Building Materials*
829 2018;160:39–47. doi:10.1016/j.conbuildmat.2017.11.030.

830 [65] Ponikiewski T, Katzer J, Bugdol M, Rudzki M. Determination of 3D porosity in steel fibre
831 reinforced SCC beams using X-ray computed tomography. *Construction and Building*
832 *Materials* 2014;68:333–40. doi:10.1016/j.conbuildmat.2014.06.064.

833 [66] Cree D, Pliya P, Green M, Noumowé A. Thermal behaviour of unstressedand stressed
834 high strength concrete containing polypropylene fibers at elevated temperature.
835 *Journal of Structural Fire Engineering* 2017;8:402–17. doi:10.1108/JSFE-07-2016-0014.

1
2
3
4
5
6
7
8
9
10
11
12
13
14
15
16
17
18
19
20
21
22
23
24
25
26
27
28
29
30
31
32
33
34
35
36
37
38
39
40
41
42
43
44
45
46
47
48
49
50
51
52
53
54
55
56
57
58
59
60
61
62
63
64
65

836 [67] Neville AM. Properties of concrete. Fifth Edit. Prentice-Hall. ISBN: 978-0-273-75580-7;
837 2011.

838 [68] Alhozaimy AM, Soroushian P, Mirza F. Mechanical properties of polypropylene fiber
839 reinforced concrete and the effects of pozzolanic materials. Cement and Concrete
840 Composites 1996;18:85–92. doi:10.1016/0958-9465(95)00003-8.

841 [69] Cifuentes H, Leiva C, Medina F, Fernández-Pereira C. Effects of fibers and rice husk ash
842 on properties of heated high-strength concrete. Magazine of Concrete Research
843 2012;64:457–70. doi:10.1680/mac.11.00087.

844 [70] Khoury GA. Polypropylene fibres in heated concrete. Part 2: Pressure relief mechanisms
845 and modelling criteria. Magazine of Concrete Research 2008;60:189–204.
846 doi:10.1680/mac.2007.00042.

847 [71] Alonso C, Fernandez L. Dehydration and rehydration processes of cement paste
848 exposed to high temperature environments. Journal of Materials Science
849 2004;39:3015–24. doi:10.1023/B:JMSE.0000025827.65956.18.

850 [72] Huang H, Wang R, Gao X. Improvement effect of fiber alignment on resistance to
851 elevated temperature of ultra-high performance concrete. Composites Part B:
852 Engineering 2019;177:107454. doi:10.1016/j.compositesb.2019.107454.

853 [73] ACI Committee 544. State of art report on fiber reinforced concrete. ACI 1R.544-96,
854 American Concrete Institute 2001.

855 [74] Li L, Zhang R, Jin L, Du X, Wu J, Duan W. Experimental study on dynamic compressive
856 behavior of steel fiber reinforced concrete at elevated temperatures. Construction and
857 Building Materials 2019;210:673–84. doi:10.1016/j.conbuildmat.2019.03.138.

858 [75] Barros JAO, Cruz JS. Fracture energy of steel fiber-reinforced concrete. Mechanics of
859 Composite Materials and Structures 2001;8:29–45. doi:10.1080/10759410119428.

860 [76] Alyhya WS, Abo Dhaheer MS, Al-Rubaye MM, Karihaloo BL. Influence of mix
861 composition and strength on the fracture properties of self-compacting concrete.
862 Construction and Building Materials 2016;110:312–22.
863 doi:10.1016/j.conbuildmat.2016.02.037.

1
2
3
4
5
6
7
8
9
10
11
12
13
14
15
16
17
18
19
20
21
22
23
24
25
26
27
28
29
30
31
32
33
34
35
36
37
38
39
40
41
42
43
44
45
46
47
48
49
50
51
52
53
54
55
56
57
58
59
60
61
62
63
64
65

864 [77] Veselý V, Sobek J, Frantík P, Seitl S. Multi-parameter approximation of the stress field in
865 a cracked body in the more distant surroundings of the crack tip. *International Journal*
866 *of Fatigue* 2016;89:20–35. doi:10.1016/j.ijfatigue.2016.02.016.

867 [78] Miarka P, Pan L, Bílek V, Seitl S, Cifuentes H. Influence of the chevron notch type on the
868 values of fracture energy evaluated on alkali-activated concrete. *Engineering Fracture*
869 *Mechanics* 2020;236:107209. doi:10.1016/j.engfracmech.2020.107209.

870 [79] Carlesso DM, de la Fuente A, Henrique S, Cavalaro SEP. Fatigue of cracked high
871 performance fiber reinforced concrete subjected to bending. *Construction and Building*
872 *Materials* 2019;220:444–55. doi:10.1016/j.conbuildmat.2019.06.038.

873 [80] Chindapasirt P, Hatanaka S, Chareerat T, Mishima N, Yuasa Y. Cement paste
874 characteristics and porous concrete properties. *Construction and Building Materials*
875 *2008;22:894–901*. doi:10.1016/j.conbuildmat.2006.12.007.

876